The January 2022 Hunga eruption cooled the southern hemisphere in 2022 and 2023

Ashok Kumar Gupta[1*], Tushar Mittal[2], Kristen E. Fauria[3], Ralf Bennartz[3], and Jasper F. Kok[1]

[1]Department of Atmospheric and Oceanic Sciences, University of California, Los Angeles, CA, 90095, USA

[2]Department of Geosciences, Pennsylvania State University, University Park, PA, USA

[3]Department of Earth and Environmental Sciences, Vanderbilt University, Nashville, TN, USA

**Corresponding author (& present Address)*: Ashok Kumar Gupta, ashokgupta@atmos.ucla.edu

Abstract

The 2022 Hunga volcanic eruption injected a significant quantity of water vapor into the stratosphere while releasing only limited sulfur dioxide. It has been proposed that this excess water vapor could have contributed to global warming, potentially pushing temperatures beyond the 1.5°C threshold of the Paris Climate Accord. However, given the cooling effects of sulfate aerosols and the contrasting impacts of ozone loss (cooling) versus gain (warming), assessing the eruption's net radiative effect is essential. Here, we quantify the Hunga-induced perturbations in stratospheric water vapor, sulfate aerosols, and ozone using satellite observations and radiative transfer simulations. Our analysis shows that these components induce clear-sky instantaneous net radiative energy losses at both the top of the atmosphere and near the tropopause. In 2022, the Southern Hemisphere experienced a radiative forcing of -0.55 ± 0.05 W m^{-2} at the top of the atmosphere and -0.52 ± 0.05 W m^{-2} near the tropopause. By 2023, these values decreased to -0.26 ± 0.04 W m^{-2} and -0.25 ± 0.04 W m^{-2}, respectively. Employing a two-layer energy balance model, we estimate that these losses resulted in cooling of about -0.10 ± 0.02 K in the Southern Hemisphere by the end of 2022 and 2023. Thus, we conclude that the Hunga eruption cooled rather than warmed the Southern Hemisphere during this period.

Introduction

On 15 January 2022, the Hunga Tonga volcano erupted from a shallow (~200 m deep) submarine vent, injecting unprecedented amounts of water vapor[1-2, 4-6] (~ 120-150 Tg) into the stratosphere. In addition, in situ and space-borne observations show that the eruption released a moderate amount of sulfur dioxide (~0.4-0.7 Tg) into the stratosphere, which was subsequently converted to sulfate aerosols over several weeks[2,4,6,9-19]. These two components, sulfate aerosol and water vapor, have opposite climate effects. Sulfate aerosols cool by scattering solar radiation, while water vapor, as a greenhouse gas, leads to stratospheric cooling and surface warming[12]. Its net radiative effect at the top of the atmosphere (TOA) depends on altitude, potentially causing either warming or cooling[12-15]. Given the unprecedented stratospheric water vapor injection, several studies have hypothesized that the Hunga eruption resulted in net climate warming[11-12]. Assessing this possibility is crucial, as volcanic-induced warming could increase the likelihood of temporarily exceeding the 1.5°C threshold set by the Paris Agreement[5] in the coming years. In contrast, past large subaerial (continental arc) eruptions—such as the 1991 Pinatubo, 1883 Krakatau, and 1815 Tambora events—led to prolonged global cooling due to the dominant influence of sulfate aerosols[18-24].

The efficacy of sulfate aerosol-induced cooling is influenced by aerosol properties such as number concentration, mass concentration, particle size distribution, and residence time[3,6,15,17], all of which substantially impact mass extinction efficiency (MEE)—a measure of an aerosol's ability to attenuate radiation per unit mass[25]. MEE depends on particle radius through two primary factors: (1) Extinction efficiency: This parameter exhibits a non-monotonic dependence on particle size, with its first peak approximately 25% greater than its second[25]. (2) Total geometric cross-section: For a fixed aerosol mass, the total geometric cross-section is inversely proportional to particle radius[25]. Consequently, smaller particles have a larger total cross-sectional area per unit mass, which enhances scattering and increases MEE.

Explosive volcanic eruptions can potentially disrupt stratospheric ozone concentrations, particularly when sulfate aerosols interact with a moist stratosphere[25-32]. Stratospheric ozone depletion leads to net cooling at Earth's TOA due to reduced shortwave absorption by ozone[22,26-37]. The climatic effects of shallow submarine eruptions can differ significantly from those of

subaerial eruptions due to variations in water vapor, SO_2, and halogen gas emissions, which influence ozone chemistry[41-43]. Thus, accurately determining the net impact of the Hunga eruption on stratospheric composition and radiative forcing is crucial. Most submarine eruptions occur in deep water and release minimal volcanic material into the atmosphere. However, the Hunga eruption—the largest shallow submarine eruption of the satellite era—offers a rare opportunity to assess the climate impacts of such events[38-40]. Thus, this requires assessing the perturbation of three key radiatively active species: water vapor, ozone, and sulfate aerosols.

Previous studies have either focused on a single atmospheric constituent or relied on simplified scaling analyses to estimate radiative forcing in the first and second years after the eruption[14,15]. This has likely contributed to conflicting conclusions, with some studies suggesting that the Hunga eruption caused warming[5], while others found it led to cooling[14,15]. For instance, Schoeberl[14] estimated a net negative (cooling) radiative forcing by combining a scaling analysis based on past subaerial eruptions (for aerosols) with radiative calculations for water vapor[43-46]. In a separate study, Schoeberl[15] applied this simplified aerosol radiative forcing scaling method to demonstrate a global reduction in downward radiative flux at the tropopause over two years, attributing this decline to changes in water vapor, aerosols, and ozone. In contrast, Jenkins[5] concluded that the Hunga eruption could contribute to global warming. However, this study only considered the impact of stratospheric water vapor (SH_2O) perturbation while neglecting the effects of aerosols, which are critical to the overall radiative balance.

Here, we conduct a comprehensive analysis of the instantaneous net radiative response to the Hunga eruption in 2022 and 2023 by: (a) Utilizing satellite remote sensing observations to quantify the spatiotemporal distribution of SH_2O, ozone, and sulfate aerosols (including their size distributions). (b) Using these observations as inputs for idealized 1D radiative transfer model simulations. Here, the model is run independently for each grid cell across the near-global domain, producing a three-dimensional output that captures both spatial and vertical variability within the stratosphere.

Results

We used space-borne remote sensing data from SAGE III[47-48] aboard the International Space Station (ISS) (solar occultation, v5.3; available since June 2017) to quantify the three-dimensional distribution of key radiatively active stratospheric species affected by the Hunga eruption: SH_2O, aerosols, and ozone (see Methods and Supplementary Figure 1). SAGE III/ISS employs a solar occultation technique, capturing up to 31 measurements daily during sunrise and sunset to generate dawn and dusk stratospheric profiles. This method requires approximately one month to cover latitudes from ~60°N to 60°S[47-48], providing detailed monthly coverage of the tropics and mid-latitudes, with seasonal variations influencing the sampling pattern. Additionally, we use multi-wavelength SAGE III/ISS observations to retrieve stratospheric aerosol particle size before and after the Hunga eruption.

For our radiative forcing analysis, we used SAGE III/ISS data due to its exceptional vertical resolution of 0.5 km. This high-resolution dataset on radiatively active species—water vapor, ozone, and aerosols—is critical for accurately estimating atmospheric heating rates and radiative forcings at the TOA and tropospause[49]. However, SAGE III/ISS data have known limitations, including a dry bias in water vapor measurements[50]. Earlier versions of SAGE III showed a ~10% dry bias in the stratosphere, which improved to ~5% in Version 5.2 and 5.3 for the mid-stratosphere[51,52]. Additionally, water vapor data below ~20 km are noisier due to aerosol and cloud interference, contributing to ~10–20% uncertainty in radiative forcing estimates, particularly in the lower stratosphere[50]. Furthermore, the infrequent sampling of aerosol extinction profiles at multiple wavelengths introduces biases in stratospheric aerosol optical depth (SAOD) estimates. To address this, we compare SAGE III-derived SAOD values with those from multiple instruments, including OMPS-NASA[53-56] (Ozone Mapping and Profiler Suite; NASA aerosol retrieval algorithms), OMPS-SASK[53-56] (Ozone Mapping and Profiler Suite; University of Saskatchewan aerosol retrieval algorithms), OSIRIS[56] (Optical Spectrograph and Infrared Imaging System), and GloSSAC[56,57] (Global Space-based Stratospheric Aerosol Climatology) (see Supplementary Figure 2).

We calculated the changes in SH_2O, sulfate aerosols, and ozone during the first and second years following the Hunga eruption ("Hunga-2022" and "Hunga-2023") relative to their

variations in the pre-eruption period (7 June 2017 – 9 December 2021; "CLIM") using SAGE-III/ISS observations. Perturbed stratospheric profiles for water vapor and aerosols from the eruption are identified as those with values exceeding two standard deviations above the background climatology. Similarly, ozone perturbations from the eruption are identified using a similar filtering criterion as described by Wilmouth[35]. To compare the SAGE-III based perturbations in SH_2O and ozone following the eruption, we used long-term (2005–2023) data from the Aura Microwave Limb Sounder (MLS[58]). Here, the absolute changes in water vapor and ozone are compared with SAGE-III observations (Supplementary Figure 3a–d for SH_2O and ozone from MLS[58]; 3e–h for SH_2O and ozone from SAGE-III).

We computed the instantaneous net (shortwave and longwave) atmospheric radiative heating rates and perturbations to the TOA and near the tropopause energy budgets using the LibRadtran[59] radiative transfer model (see Supplementary Figure 1 and Methods). These energy budget perturbations serve as proxies for the overall atmospheric energy balance, accounting for the contributions of stratospheric water vapor, ozone, and sulfate aerosols. In the following sections, we first examine the individual radiative effects of each perturbed species before analyzing their combined net impact.

Changes in stratospheric water vapor after Hunga eruption

We show the absolute changes in the zonal-mean latitude-altitude variations of stratospheric H_2O mixing ratio between the (Fig. 1a) "Hunga-2022" and "CLIM" periods and (Fig. 1b) "Hunga-2023" and "CLIM" periods based on the SAGE III/ISS observations.

We observe that the SH_2O injected by the Hunga eruption spread throughout the middle stratosphere from the southern mid-latitudes to the northern tropics during the first year (Fig. 1a). Around the eruption latitude (20°S–0°S latitude), we observed a 2 km thick layer, extending from 27 to 29 km, with a 90% enhancement in SH_2O mixing ratio relative to the background climatology (Fig. 1a and Supplementary Figure 4a). Further south, from 20°S to 50°S, the increase in stratospheric water vapor mixing ratio was more modest, indicating lower concentrations of water vapor due to its latitudinal transport by stratospheric wind patterns. The near-global SH_2O content map, integrated from the lower to the upper stratosphere (up to an

altitude of 45 km), shows a noticeable absolute increase of approximately 0.5–1 g m^{-2} in the SH (Fig. 1c).

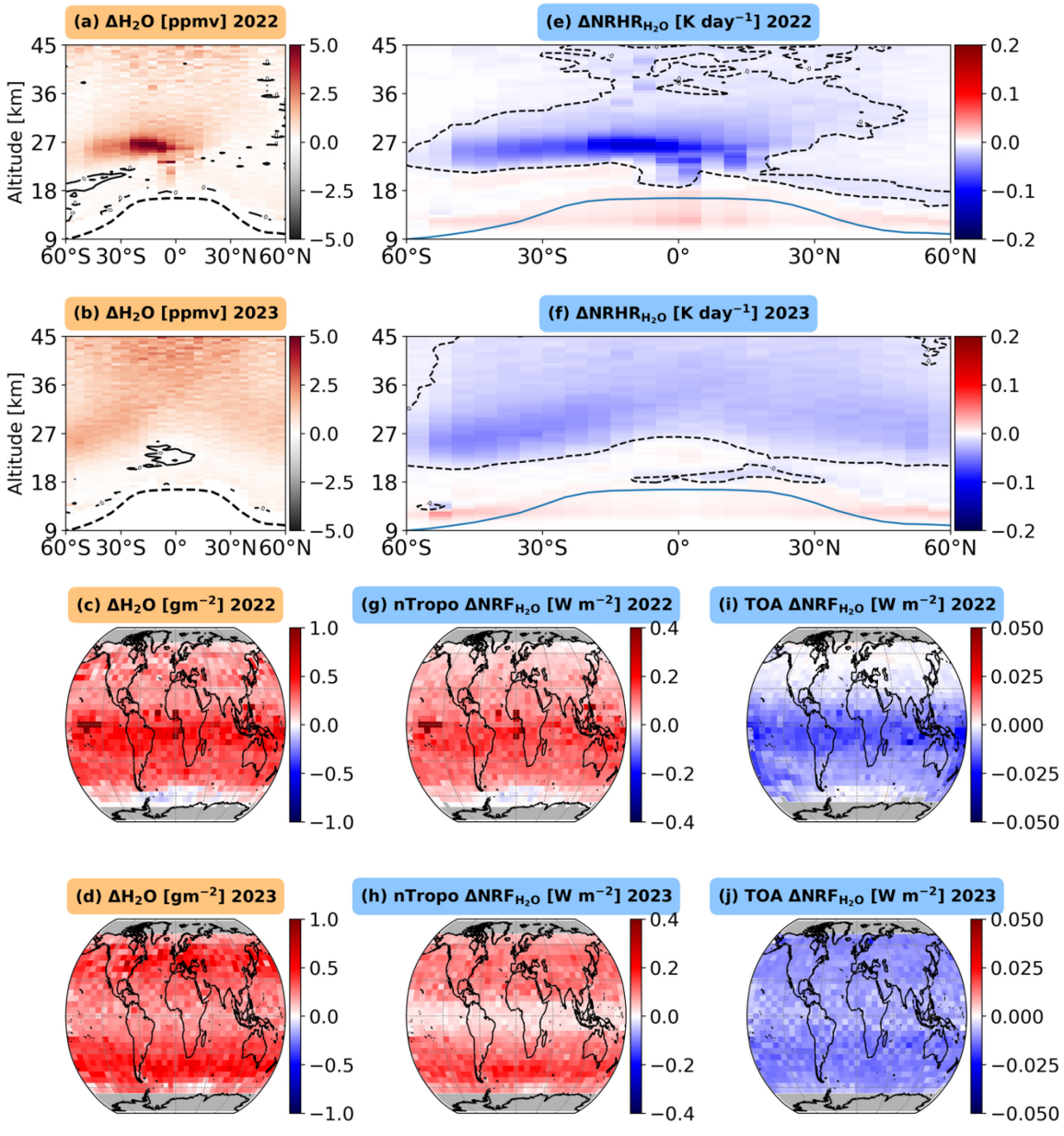

Figure 1: Observed enhancement of stratospheric water vapor and the associated simulated instantaneous radiative forcing during 2022 and 2023 following the Hunga eruption. *Panels* ***(a)*** *and* ***(b)*** *show the zonal- and annual-mean latitude–altitude variation in the change of the stratospheric water vapor (H_2O) mixing ratio [ppmv] for 2022 and 2023, respectively, relative to the reference climatology (CLIM) period from 2017 to 2021. Contours denote near-zero changes, and the dashed black line represents the tropopause height. Panels* ***(c)*** *and* ***(d)*** *show the*

*corresponding vertically integrated changes from the lower stratosphere to the upper stratosphere. Panels (**e**) and (**f**) show the latitude–altitude distribution of the difference in net (longwave + shortwave) radiative heating rates (ΔNRHR; K day^{-1}) of water vapor within the stratosphere between each post-eruption year and the CLIM period. Panels (**g**) and (**h**) depict changes in near-tropopause net radiative forcing (ΔNRF_{H_2O}; W m^{-2}) for 2022 and 2023, highlighting perturbations primarily observed near the lowest levels of the lower stratosphere (above the tropopause height). Panels (**i**) and (**j**) show the changes at the top-of-atmosphere (TOA) net radiative forcing (ΔNRF_{H_2O}; W m^{-2}) for 2022 and 2023, respectively.*

In the second year (2023) following the eruption, the injected SH_2O has spread from the southern to the northern hemisphere, covering the middle to the upper stratosphere. The substantial dispersion of SH_2O during the second year has led to a decrease in its mixing ratio and concentration (Fig. 1b, d; see relative changes in SH_2O in Supplementary Figure 4a, b). This accumulated SH_2O has reduced by around 10% relative to the first year, as observed from SAGE-III (Fig. 1d; Table 1). The widespread vertical distribution of SH_2O in 2023, in contrast to 2022, is attributed to the stratospheric Brewer-Dobson circulation in combination with some perturbations in stratospheric circulation patterns due to stratospheric temperature perturbations following the Hunga eruption[33,38].

We also quantify the impact of the 2022 Hunga eruption on the seasonal timeline of changes in SH_2O concentration from 2022 to 2023, compared to its seasonal 5-year climatology value between 2017 and 2021 (Fig. 2a). We observe a distinct increase in SH_2O concentration from January 2022 onwards from SAGE-III observations. The peak in absolute changes in SH_2O concentration value is approximately 0.5 g m^{-2} (30% higher relative to the background value) in the SH during spring season (MAM) of 2022 (Fig. 2a). The increase in SH_2O gradually decreases in the summer (JJA) and autumn (SON) of 2022 and other seasons of 2023. Note that the decrease in SH_2O concentration in the SH from 2022 to 2023 is minimal with a decline of around 10-15% (Fig. 2a). The NH and near-global domain also experience a substantial increase in the magnitude of SH_2O in 2022 and 2023. The strong vertical transport of tropical middle stratosphere SH_2O into the upper stratosphere and towards mid- and high-latitudes regions in

2023 in the SH and NH are attributed to Brewer-Dobson circulation[33,38,46], as evident from the vertical and spatial map of SH_2O in Fig. 1a-d.

Net radiative heating rate and radiative forcing of the Hunga-perturbed SH_2O: 2022 versus 2023

We used idealized radiative transfer model simulations (see Methods) to assess the stratospheric radiative heating rates (Fig. 1e, f) and radiative forcing of the perturbed SH_2O near the tropopause (Fig. 1g, h) and at the TOA (Fig. 1i, j). In 2022, in the middle stratosphere (24-26 km) around the eruption latitude, the additional SH_2O caused a cooling of -0.20 K day^{-1} due to enhanced emission of longwave radiation (Supplementary Figure 5a). This cooling was partially offset by heating of up to +0.05 K day^{-1} from the additional absorption of SW radiation by the SH_2O (Supplementary Figure 5g). These effects combined to produce a net radiative cooling rate of up to -0.15 K day^{-1} (dark blue color in Fig. 1e). During 2023, the vertical spreading of the SH_2O layer in both hemispheres exhibited a net cooling effect below -0.1 K day^{-1} (Fig. 1f).

During 2022 and 2023, the SH_2O perturbation in the middle and upper stratosphere following the eruption substantially affected the clear-sky net instantaneous radiative forcing near the tropopause (Fig. 1g, h) and at the TOA (Fig. 1i, j) relative to background climatology. Enhanced SH_2O, a potent greenhouse gas, substantially increases downward longwave radiation emission from the water vapor layer, contributing to a higher net radiative forcing within Earth's atmosphere while having minimal impact on shortwave radiation (Supplementary Figure 5g-l). We find that the Hunga eruption's impact on SH_2O in 2022 increased the net radiative flux by $+0.12 \pm 0.01$ Wm^{-2} near the tropopause in the SH and $+0.10 \pm 0.01$ Wm^{-2} in the near-global domain (Table 1). In contrast, at Earth's TOA, the enhanced SH_2O in 2022 decreased the net radiative flux by $\sim -0.010 \pm 0.001$ Wm^{-2} in the SH and $\sim -0.008 \pm 0.001$ Wm^{-2} in the near-global domain (Table 1). This is due to the enhanced longwave radiation emission from water vapor in the upper stratosphere.

During the summer of 2022, we quantified a peak positive instantaneous net radiative flux of $+0.15 \pm 0.02$ Wm^{-2} near the tropopause and a negative instantaneous net radiative flux of -0.014 ± 0.001 Wm^{-2} at TOA in the SH, driven by enhanced SH_2O (Fig. 2e, i). In the SH, the

increased positive net instantaneous radiative flux of +0.15 ± 0.02 Wm^{-2} near the tropopause contributed to a surface warming of +0.015 K ± 0.004 K by the end of 2022, as estimated using the FaIR[7-8] simple two-layer energy balance climate emulator (see Methods; light cyan color in Supplementary Figure 6e). The increased net instantaneous radiative forcing and its associated uncertainty near the tropopause and at the TOA are calculated solely based on changes in SH_2O, assuming a constant background temperature profile for both pre- and post-eruption periods. Notably, these calculations do not explicitly account for the influence of clouds and temperature adjustments, which may lead to an underestimation of uncertainties.

In 2023, Hunga-perturbed SH_2O increased the net radiative flux near the tropopause by +0.09 ± 0.01 Wm^{-2} in the SH and +0.08 ± 0.01 Wm^{-2} in the NH. These changes in radiative flux led to a mean surface warming of +0.022 ± 0.003 K in the SH and +0.017 ± 0.002 K in the NH (see blue and cyan colors in Supplementary Figure 6e). At Earth's TOA, Hunga-perturbed SH_2O decreased the net instantaneous radiative flux by -0.01 ± 0.001 Wm^{-2} in the SH and -0.009 ± 0.001 Wm^{-2} in the near-global domain.

In aggregate, the SH_2O in the first year (2022) and second year (2023) following the eruption contributed to increased radiative forcing near the tropopause and decreased radiative forcing at Earth's TOA, primarily in the SH, but without a strong longitudinal pattern (Fig. 1c, g, i). In 2023, the widespread dispersion of SH_2O led to tropospheric warming near the tropopause in both hemispheres (Fig. 1d, h).

The spread of stratospheric water vapor is driven by the Brewer–Dobson circulation, a large-scale atmospheric circulation pattern that transports tropical tropospheric air into the stratosphere, followed by its poleward movement and descent at higher latitudes[6,46]. Furthermore, the perturbed water vapor levels may influence this background circulation. A more detailed investigation of these interactions would require the application of advanced climate modeling, which is beyond the scope of this study.

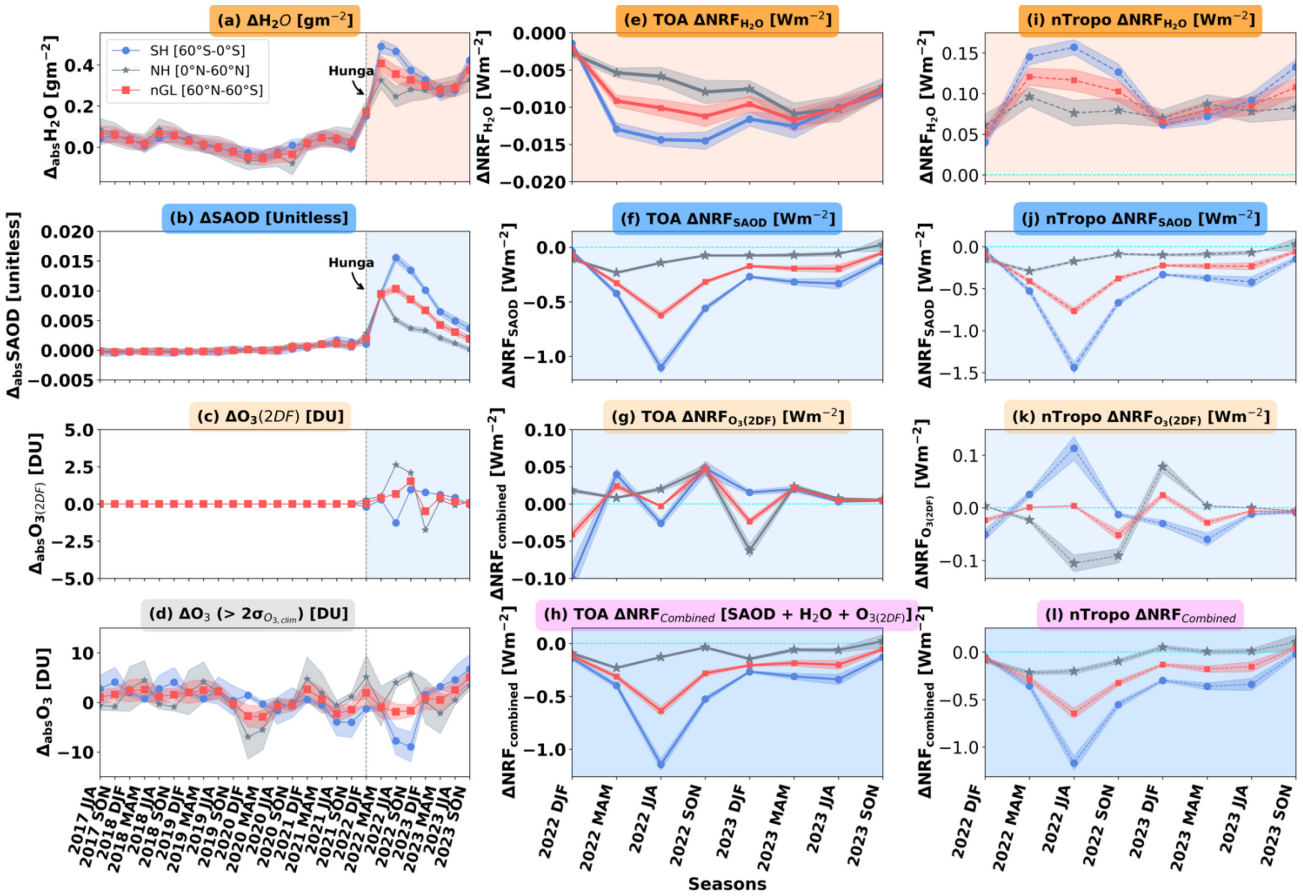

Figure 2: Evolution of the absolute changes and corresponding top-of-atmosphere (TOA) and near-tropopause instantaneous net radiative forcing (ΔNRF) of three radiatively important stratospheric species perturbed by the Hunga eruption. *Panels* ***(a)–(d)*** *show the evolution of the seasonal mean absolute changes (relative to the reference climatology [CLIM] period) from 2017 until 2023 for:* ***(a)*** *stratospheric water vapor (SH_2O) concentration,* ***(b)*** *stratospheric aerosol optical depth (SAOD), (c) ozone concentration (with 2D-filtered condition), and* ***(d)*** *ozone concentration (unfiltered, showing values exceeding 2σ above background climatology, UNF). These values are presented for the Southern Hemisphere (SH; blue line), the Northern Hemisphere (NH; grey line), and near-global (60°S–60°N; nGL; red line). Panels* ***(e)–(h)*** *show the clear-sky net (longwave plus shortwave) radiative forcing (ΔNRF) at TOA due to post-eruption perturbations in:* ***(e)*** *SH_2O,* ***(f)*** *SAOD,* ***(g)*** *ozone (2D-filtered; 2DF), and* ***(h)*** *the combined effect of SH_2O + SAOD + ozone (2D-filtered). Panels* ***(i)–(l)*** *show the corresponding dashed blue, grey, and red lines indicate the clear-sky ΔNRF near the tropopause. Dashed cyan lines indicate the horizonal bar near zero in* ***(e-h)*** *and* ***(i-l)****. Shaded regions represent the interannual standard deviation (1σ) of the background values (except for 2D-filtered ozone,*

which is extracted above 2σ; see Methods). The perturbations in SH_2O, SAOD, and ozone (2D-filtered) following the eruption exceed their interannual variability, resulting in the combined instantaneous radiative forcing shown in panel ***(l)****.*

Changes in stratospheric aerosols after the Hunga eruption

The Hunga eruption injected not only a substantial amount of water vapor but also a moderate quantity of sulfur dioxide (SO_2) into the stratosphere, estimated at approximately 0.4–0.7 Tg[14,15,60]. The total SO_2 transported from the troposphere to the stratosphere is estimated to be around 1 Tg[60]. However, compared to previous volcanic eruptions such as Raikoke in 2019 (1.5 Tg[61,62]) and the Pinatubo eruption in 1991 (~17 Tg[63]), the amount of SO_2 injected into the stratosphere by the Hunga eruption was considerably smaller.

To quantify the impact of the Hunga eruption on the stratosphere, we identified perturbed aerosol extinction in 2022 and 2023 by detecting deviations exceeding above two standard deviations (σ) from the background climatology. This method is based on the expectation that, under normal conditions, stratospheric aerosol extinction remains relatively stable; therefore, any significant deviation likely reflects the additional aerosol load injected by the eruption, which in turn influences radiative forcing and stratospheric dynamics[62]. This approach allowed us to assess the three-dimensional distribution of perturbed stratospheric aerosol extinction and the associated SAOD. We observed an enhanced aerosol extinction of solar radiation over 50°S–20°N in the stratosphere at 22–24 km altitude in 2022 following the eruption (Fig. 3a), with a maximum relative increase in aerosol extinction reaching 800% (Supplementary Fig. 4a). The near-global SAOD map, which represents integrated aerosol extinction from the lower to the upper stratosphere (Fig. 3c), reveals a substantial absolute increase of approximately +0.014 ± 0.001 in the SH in 2022 (Fig. 3c; Fig. 2b; Table 1). Similar to SH_2O, stratospheric aerosols are predominantly concentrated in the SH, exhibiting no strong longitudinal pattern (Fig. 3c). During the second-year post-eruption (2023), we observe a decrease in 521 nm sulfate aerosol extinction from 0.004 km^{-1} to 0.002 km^{-1} between 50°S and 20°N, at altitudes ranging from 10 km in the southern midlatitudes to 25 km in the tropics (Fig. 3b).

Unlike water vapor, the spread of SAOD is predominantly confined to the SH (Fig. 3c,d). In 2023, perturbed SAOD decreased by around 50% compared to the first-year aerosol perturbation (Fig. 2b; Fig. 3c, g). With minimal aerosol perturbation in the NH, the cooling impact of SAOD in the SH contributes to a hemispheric asymmetry under idealized conditions. The reduction in SAOD observed in 2023 could be attributed to the gravitational settling of stratospheric sulfate aerosols[64,65].

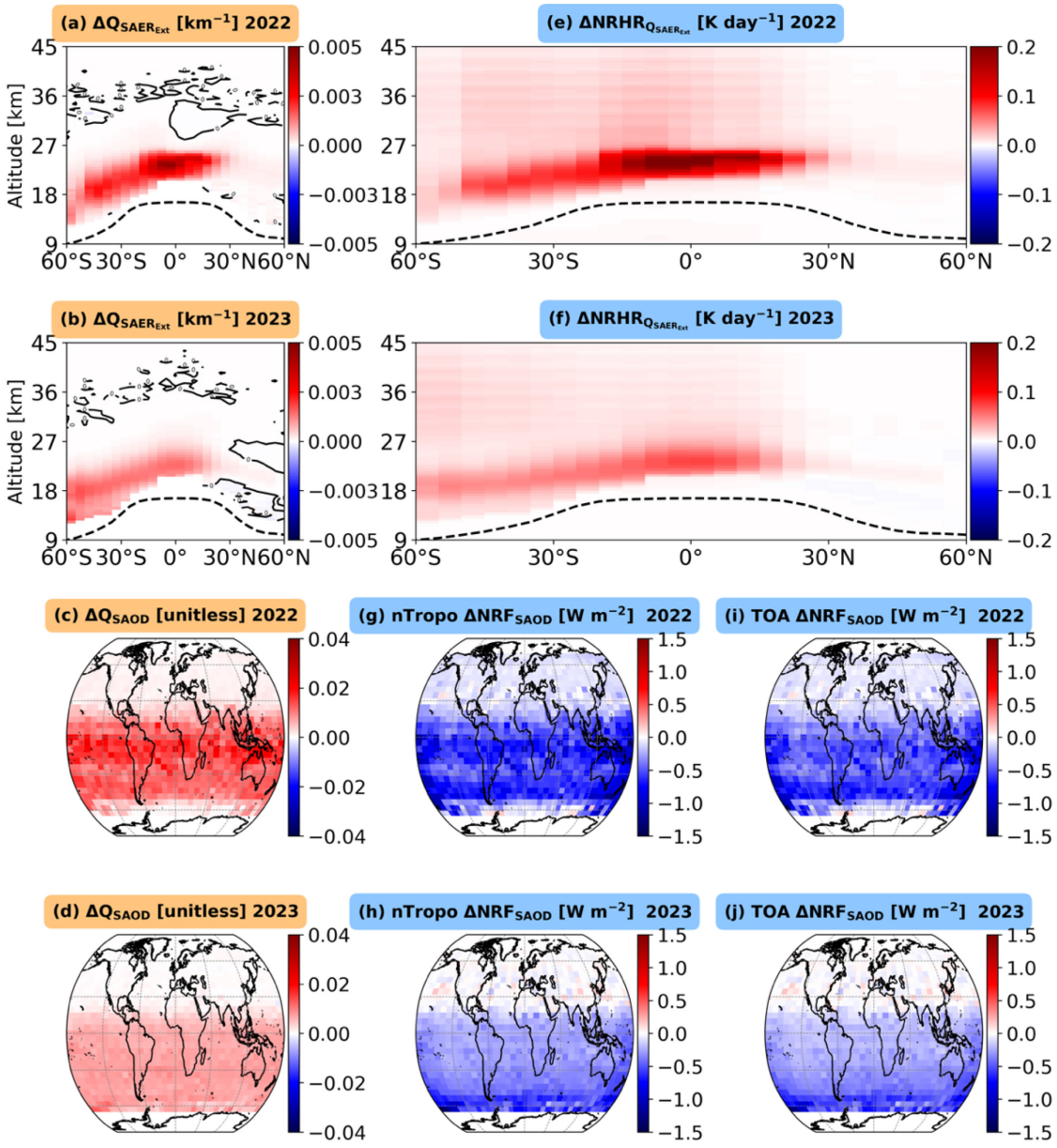

Figure 3: Observed enhancement of stratospheric aerosol and the associated simulated instantaneous radiative effects during 2022 and 2023 following the Hunga eruption. *Panels*

*(**a**) and (**b**) show the zonal- and annual-mean latitude–altitude variation in the change of the aerosol extinction coefficient at 521 nm ($Q_{SAERext}$; km^{-1}) for 2022 (15 Jan 2022 to 14 Jan 2023) and 2023 (15 Jan 2023 to 31 Dec 2023), respectively, relative to the reference climatology (CLIM) period from 07 June 2017 to 09 Dec 2021. Contours denote near-zero changes, and the dashed black line represents the tropopause height. Panels (**c**) and (**d**) display the vertically integrated aerosol extinction coefficient (SAOD) for the perturbed lower to upper stratosphere. Panels (**e**) and (**f**) show the latitude–altitude distribution of the difference in net (longwave + shortwave) radiative heating rates (ΔNRHR; K day^{-1}) of stratospheric aerosol between each post-eruption year and the CLIM period. Panels (**g**) and (**h**) depict the changes in near-tropopause net radiative flux (ΔNRF_{SAOD}; W m^{-2}) for 2022 and 2023, respectively, highlighting perturbations primarily observed in the lowest levels of the lower stratosphere (above the tropopause height). Panels (**i**) and (**j**) show the corresponding changes in the top-of-atmosphere (TOA) net radiative flux (ΔNRF_{SAOD}; W m^{-2}) for 2022 and 2023, respectively.*

During 2022, following the eruption, we retrieved a mean effective radius of sulfate aerosols of approximately 0.3 µm (with a median of 0.27 µm) in the mid-stratosphere (Table 1 and Supplementary Fig. 7a,e), which is consistent with the findings of Knepp[66]. In 2023, the mean effective radius of sulfate aerosols in the SH was 0.29 µm (Table 1 and Supplementary Fig. 7i,m), nearly identical to that observed in 2022. Boichu[17] and Khaykin[67] showed that during the first two months after the eruption, sulfate aerosol particles were larger; over time, these particles decreased in size, transitioning to finer particles.

We compare the annual mean percentage change in near-global ΔSAOD for 2022, derived from SAGE III, with OMPS-NASA[56], OMPS-SASK[56], OSIRIS[56], and GloSSAC[56] to assess biases (Supplementary Fig. 2; Table 1). Among datasets, OMPS-NASA has the largest ΔSAOD discrepancy (-66.5%), followed by OMPS-SASK (-37.8%), OSIRIS (-12.6%), and SAGE-III/ISS (-15.5%), while GloSSAC shows a slight increase (+1.8%). Despite inter-instrument biases, GloSSAC estimates align well with our SAOD approach based on >2σ perturbations. These differences highlight the need for multi-instrument comparisons to refine SAOD estimates and radiative forcing assessments post-eruption. OMPS-NASA shows a >50%

high bias due to its fixed aerosol size assumption, while OMPS-SASK mitigates this by accounting for size variations[54].

Net radiative heating rate and radiative forcing of the Hunga-perturbed stratospheric sulfate aerosol: 2022 versus 2023

We present the near-global distribution of changes in net radiative flux near the tropopause (Fig. 3g) and at the TOA (Fig. 3i) resulting from the perturbation of sulfate-dominated stratospheric aerosols within the lower-to-middle stratosphere. During 2022, when averaged over the SH, our results indicate that the mean net radiative flux at Earth's TOA decreased by 0.53 ± 0.04 W m^{-2}, leading to a surface cooling of 0.07 ± 0.01 K, as estimated from the FaIR[7,8] model (Supplementary Fig. 6b). This reduction is attributed to an increase in SAOD (i.e., ΔSAOD) of approximately 0.014 ± 0.001 (Fig. 2b; Fig. 3c; Table 1). Similarly, the mean net radiative flux near the tropopause in the SH decreased by 0.66 ± 0.05 W m^{-2} (Fig. 2b; Fig. 3g; Table 1), resulting in a surface cooling of 0.09 ± 0.01 K (Supplementary Fig. 6f). On a near-global scale, the mean radiative flux changes at the TOA and near the tropopause are estimated to be -0.34 ± 0.03 W m^{-2} and -0.41 ± 0.04 W m^{-2}, respectively, associated with a ΔSAOD of around 0.008 ± 0.001 (Fig. 2b,f, j; Fig. 5a; Table 1).

During 2023, the increase in SAOD associated with the Hunga eruption amounted to 0.007 ± 0.001 in the SH, leading to a reduction in net radiative flux at the TOA and near the tropopause by 0.26 ± 0.03 W m^{-2} and 0.31 ± 0.04 W m^{-2}, respectively. Consequently, surface temperatures cooled by around 0.11 ± 0.01 K by the end of the year. The system's thermal inertia helped sustain this cooling, similar to the radiative forcing changes observed in 2022. On a near-global scale, an increase in SAOD of 0.005 ± 0.001 resulted in a reduction in net radiative flux of 0.15 ± 0.03 W m^{-2} at the TOA and 0.19 ± 0.04 W m^{-2} near the tropopause (Fig. 2b,f, j; Fig. 5a,b; Table 1).

Using the above results at TOA, we estimate a radiative forcing efficiency (near-global mean radiative forcing at TOA per unit SAOD) of approximately 25–40 Wm^{-2} during 2022 and 2023. This estimate is relatively higher than those reported by Marshall[68] and Schmidt[69] for other subaerial volcanic eruptions.

We retrieved sulfate aerosol effective radii of approximately 0.3 μm (with a median radius of 0.27 μm) using Mie theory (see Methods), which indicates that these aerosols scatter incoming solar radiation most efficiently per unit mass[65]. This enhanced scattering efficiency may have contributed to the higher radiative forcing efficiency observed for sulfate aerosols, highlighting the need for further chemistry-based sensitivity analyses of radiative efficiency in future studies.

Our estimated effective (median) radius of sulfate aerosols has a mean value of 0.3 μm (0.27 μm). These particle sizes result in a high sulfate MEE (Table 1; Supplementary Fig. 7d, h, l, p and Supplementary Fig. 8), thereby enhancing sulfate aerosol forcing. The calculated MEE and its associated standard deviation are 4.21 ± 0.13 $m^2\ g^{-1}$ (4.24 ± 0.13 $m^2\ g^{-1}$) in the SH, 4.22 ± 0.17 $m^2\ g^{-1}$ (4.17 ± 0.17 $m^2\ g^{-1}$) in the NH, and 4.21 ± 0.25 $m^2\ g^{-1}$ (4.21 ± 0.25 $m^2\ g^{-1}$) for the near-global domain during 2022 (2023), respectively (Table 1).

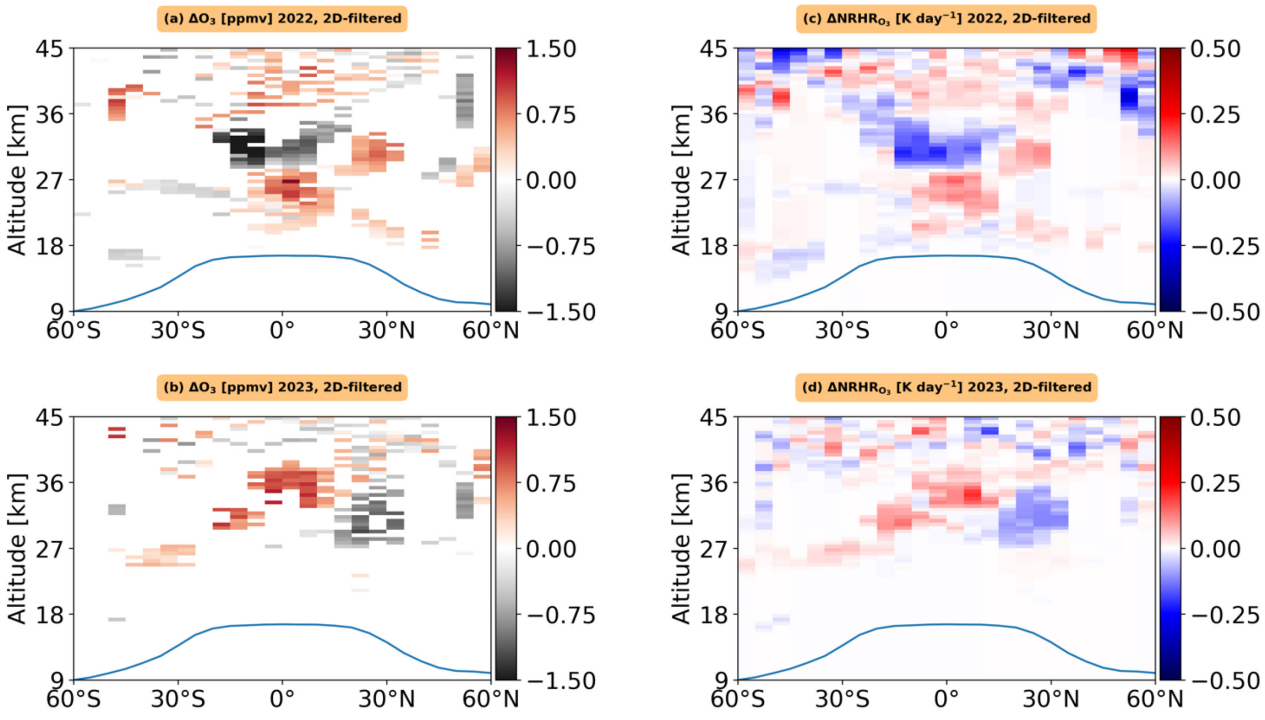

Figure 4: Observed 2D-filtered changes in stratospheric ozone mixing ratios and the associated simulated instantaneous radiative forcing during 2022 and 2023 following the Hunga eruption. *Panels (a) and (b) show the zonal- and annual-mean latitude–altitude variation of the changes in stratospheric ozone mixing ratios for 2022 and 2023, respectively.*

Panels (c) and (d) present the latitude–altitude distribution of the differences in net (longwave + shortwave) radiative heating rates (ΔNRHR) for stratospheric ozone for 2022 and 2023, respectively.

Changes in stratospheric ozone after the Hunga eruption: 2D-Filtered technique

Following the methodologies of Wilmouth[35] and Santee[37], we assessed changes in the ozone mixing ratio in 2022 and 2023 relative to background mean values using both SAGE III[47] and MLS[58] datasets. To better quantify the impact of the Hunga eruption, we applied a 2D-filtered (2DF) technique (see Methods) to distinguish changes in the zonal-mean mixing ratio. Using the 2DF technique, the extent of the Hunga eruption's influence on ozone fluctuations becomes discernible, as the observed changes following the eruption exceed the typical year-to-year variability seen before the event (Fig. 2c).

We find a slightly stronger negative ozone mixing ratio anomaly, with values of around -0.5 ppmv at 27 km and -1 ppmv at 32 km in the SH during the summer of 2022 (Fig. 4a; Fig. 2c; Supplementary Fig. 9c). In 2023, we also observe an increase in the ozone mixing ratio anomaly, with values exceeding 0.5 ppmv between 22 km and 36 km altitude near equatorial regions and in the SH (Fig. 4b; Fig. 2c; Supplementary Fig. 9i, j).

Wilmouth[35], Wang[36], and Santee[37] conducted a thorough analysis of various trace gas species and also used global climate model simulations to determine the mechanism behind the potential ozone loss in 2022. The results of their study demonstrate that the eruption impacted ozone by influencing both stratospheric dynamics and ozone chemistry. We note that to exactly pinpoint the physical mechanism related to the effects of the Hunga eruption on ozone gain in 2023, detailed modeling studies coupling stratospheric dynamics and chemistry are needed which is out of the scope of this study. Therefore, our primary results are focused on assessing the influence of radiative forcing of water vapor, SAOD and ozone (2D-Filtered technique).

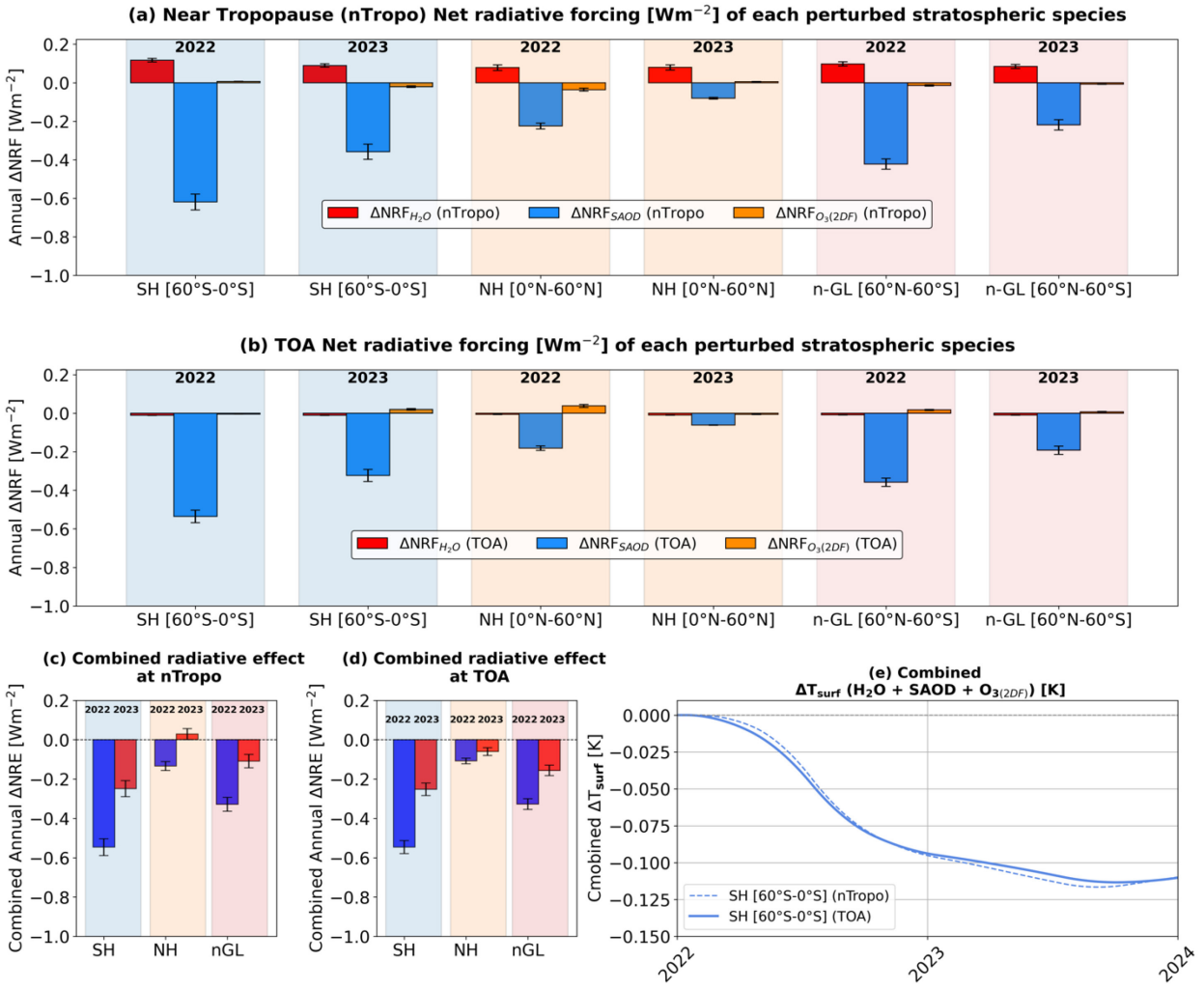

Figure 5: Net radiative forcing during 2022 and 2023 due to three radiatively important stratospheric species perturbed by the Hunga eruption. *Panel (a) shows the clear-sky net (longwave + shortwave) instantaneous radiative forcing near the tropopause due to perturbations in stratospheric H_2O (red bars), aerosols (blue bars), and O_3 (orange bars) for the Southern Hemisphere (SH), Northern Hemisphere (NH), and near-global (60°S–60°N) regions. Panel (b) presents the clear-sky net instantaneous radiative forcing at the top-of-the-atmosphere (TOA) for the same species and regions. Panels (c) and (d) show the combined ΔNRF near the tropopause and at the TOA, respectively, averaged for the SH, NH, and near-global regions during 2022 and 2023. Panel (e) shows the surface temperature changes in the SH, estimated using a two-layer energy balance FaIR model based on the perturbed instantaneous energy balance at the TOA and near the tropopause. These estimates represent only a first-order approximation of the actual surface*

temperature changes. Uncertainty bars (black) in panels (a) and (c) indicate the background interannual variations in the radiative forcing for SH_2O, SAOD, and O_3 (black caps).

Net radiative heating rate and radiative forcing of the Hunga-perturbed stratospheric ozone (2D-Filtered): 2022 versus 2023

Because ozone molecules absorb a substantial amount of solar radiation, a decrease in their concentration would lead to reduced warming within the stratosphere. This, in turn, would decrease the upwelling solar radiation from the uppermost layer of the stratosphere, resulting in a relative reduction in the net radiative flux at Earth's TOA[33]. The opposite effect occurs in the case of ozone gain.

We find that the ozone mixing ratio, derived from the 2D-filtered technique, decreased in the stratosphere over 20°S–40°S between 24–27 km altitude and over 10°S–30°S between 30–35 km altitude during the first year after the eruption (Fig. 4a). This ozone loss contributed to stratospheric cooling of more than -0.15 K day^{-1} (Fig. 4c). Additionally, we observed an increase in ozone in the equatorial regions (15°S–15°N) in the lower stratosphere below 27 km (Fig. 4a), leading to stratospheric warming of more than +0.1 K day^{-1} (Fig. 4c). We observed a strong increase in ozone mixing ratio from the middle stratosphere to lower stratosphere in 2023, possibly influenced by dynamical processes associated with the easterly phase of the Quasi-Biennial Oscillation and secondary stratospheric circulation[15,32-36], contributing to a stratospheric heating rate of approximately +0.15 to +0.2 K day^{-1}.

During 2022, we found that the reduction in O_3 concentration was primarily located in the SH (Table 1). This decline in stratospheric ozone concentration by -0.06 DU in the SH contributed to a small negative net radiative flux of -0.009 W m^{-2} at the TOA and a positive net radiative flux of +0.018 W m^{-2} near the tropopause (Table 1). During 2023, an increase in ozone concentration by 1.38 DU in the NH resulted in a net positive radiative flux change of +0.02 ± 0.01 W m^{-2} at the TOA and -0.05 ± 0.01 W m^{-2} near the tropopause (Table 1).

Hunga eruption-perturbed species	SH		NH		nGL	
	2022	2023	2022	2023	2022	2023
$r_{eff}{}_{HTHH}[\mu m]$	0.30	0.29	0.26	0.27	0.28	0.28
$MEE_{HTHH}[m^2 g^{-1}]$	4.21	4.24	4.22	4.17	4.21	4.21
$M_{SO_2{}_{HTHH}}[Tg]$	0.46	0.31	0.26	0.19	0.71	0.50
$SAOD_{HTHH}[Unitless]$	0.017	0.013	0.010	0.007	0.013	0.010
$\Delta M_{SO_2{}_{HTHH}}[Tg]$	0.35	0.18	0.13	0.06	0.48	0.24
$\Delta SAOD_{HTHH}$ $[Unitless]$	0.014	0.007	0.005	0.002	0.008	0.005
$\Delta NRF_{SAOD}\ [Wm^{-2}]$ *(near tropopause)*	**-0.66**	**-0.31**	**-0.18**	**-0.06**	**-0.41**	**-0.19**
$\Delta NRF_{SAOD}\ [Wm^{-2}]$ *(TOA)*	**-0.53**	**-0.26**	**-0.14**	**-0.05**	**-0.34**	**-0.15**
$\Delta H_2O_{Total}\ [Tg]$	86	72	59	66	145	138
$\Delta H_2O\ [gm^{-2}]$	0.37	0.32	0.24	0.30	0.32	0.31
$\Delta NRF_{H_2O}[Wm^{-2}]$ *(near tropopause)*	**0.12**	**0.09**	**0.08**	**0.08**	**0.10**	**0.08**
$\Delta NRF_{H_2O}[Wm^{-2}]$ *(TOA)*	**-0.010**	**-0.01**	**-0.005**	**-0.009**	**-0.008**	**-0.009**
ΔO_3 *[DU] (2DF with* H_2O*)*	-0.06	0.45	1.38	-0.36	0.66	0.05
$\Delta NRF_{O_3}[Wm^{-2}]$ *(2DF; near tropopause)*	**0.018**	**-0.028**	**-0.05**	**0.02**	**-0.018**	**-0.004**
$\Delta NRF_{O_3}[Wm^{-2}]$ *(2DF; TOA)*	**-0.009**	**0.01**	**0.02**	**-0.006**	**0.007**	**0.002**
Near tropopause $\Delta NRF_{H_2O+SAOD+O_{3,2DF}}$	**-0.52**	**-0.25**	**-0.15**	**+0.04**	**-0.33**	**-0.11**
At TOA $\Delta NRF_{H_2O+SAOD+O_{3,2DF}}$	**-0.55**	**-0.26**	**-0.13**	**-0.07**	**-0.34**	**-0.16**

Table 1: Properties and hemispherical mean net radiative forcing of radiatively important stratospheric species perturbed by the 2022 Hunga eruption. *The blue rows list the mean*

effective radius (r_{eff}; in µm) of retrieved sulfate aerosols, the retrieved vertically integrated SO_2 mass (MSO_2; in Tg), the retrieved mass extinction efficiency (MEE; in $m^2\ g^{-1}$) per gram of SO_2, and the SAGE-III/ISS observed SAOD for Hunga for the Southern Hemisphere (SH), Northern Hemisphere (NH), and near-global (n-GL) domains for 2022 and 2023. The light orange rows present the retrieved absolute (Hunga–CLIM) change in sulfate aerosols (ΔMSO_{2Hunga}; Tg), the SAGE-III/ISS observed absolute (Hunga–CLIM) changes in the vertically integrated SAOD (ΔSAOD), and the resulting simulated mean net radiative forcing (ΔNRF_{SAOD}; W m^{-2}) near the tropopause and at the top of the atmosphere (TOA). The dark orange rows show the SAGE-III/ISS observed total injected H_2O mass (ΔH_2O; Tg) and its corresponding simulated mean net radiative forcing (ΔNRF_{H_2O}; W m^{-2}) near the tropopause and at the TOA. The light magenta rows display the absolute changes in ozone derived from the 2D-filtered technique (ΔO_3; DU; 2DF with water vapor) and their simulated mean net radiative forcing (ΔNRF_{O_3}; W m^{-2}; 2DF) near the tropopause and at the TOA. The final grey rows show the combined net radiative forcing of the three species ($NRF_{H_2O+SAOD+O_{3,2DF}}$; W m^{-2}) near the tropopause and at the TOA.

The combined net radiative effects of the three perturbed stratospheric species

After determining the domain-averaged net instantaneous radiative effects of enhanced stratospheric water vapor, stratospheric sulfate aerosol, and ozone using the 2D-filtered technique, we combined these three radiative perturbations to estimate the net TOA radiative forcing and the associated surface temperature changes due to the eruption (Fig. 5; Table 1). Using a simple climate emulator (FaIR)[7-8], we find that the Hunga eruption induced a mean surface cooling effect of approximately -0.10 ± 0.01 K by the end of 2022 (Fig. 5e). This cooling resulted from a combined instantaneous radiative forcing of ~-0.55 ± 0.05 W m^{-2} at the TOA, concentrated almost entirely in the SH (Fig. 4c; Table 1). This cooling effect was primarily driven by sulfate aerosols. During 2023, in the SH, the combined effects of SH_2O, SAOD, and ozone (O_3-2DF) resulted in a TOA radiative forcing of -0.26 ± 0.04 W m^{-2}, leading to a cooling of -0.10 ± 0.01 K by the end of 2023 (Fig. 5d). Thus, the Hunga-associated cooling (and any potential future warming) is likely very small compared to natural climate variability and will be difficult to detect observationally.

583 The stronger surface cooling observed in both 2022 and 2023, despite variations in the
584 magnitude of the combined net radiative flux at the TOA and near the tropopause altitude,
585 suggests a cumulative effect of radiative forcing over time, influenced by thermal inertia and
586 feedback processes. This implies that, although radiative forcing in 2023 was relatively small,
587 the temperature change in 2023 also reflects the residual effects of the stronger forcing from
588 2022, leading to a similar overall temperature response.
589
590 Also, given that the Pinatubo eruption injected approximately 20 Tg of sulfur, resulting in
591 a maximum cooling of about –0.5 K, a simple linear scaling suggests that the HTHH event,
592 which injected less than 1 Tg of sulfur, would induce a cooling effect of approximately –0.025
593 K[15,22]. Such a small temperature change is likely to be masked by natural variability and may not
594 be directly detectable. Given the modest magnitude of the expected cooling, further investigation
595 using comprehensive climate model simulations is necessary to determine whether these
596 gradients could trigger any measurable atmospheric responses.
597
598 In conclusion, our findings indicate that the Hunga eruption did not cause warming in
599 the SH or globally between 2022 and 2023. Instead, it had a cooling effect in the SH.
600 The efficient conversion of SO_2 into sulfate aerosols in a water-rich stratosphere in the SH likely
601 contributed to the net cooling effect observed at Earth's TOA in 2022 and 2023.
602
603 However, in 2023, we find a slight increase in net radiative flux near the tropopause in
604 the NH, primarily due to increased SH_2O and reduced ozone, with minimal perturbation of
605 SAOD. Given that the stratospheric lifetime of SH_2O is much longer than that of SAOD (around
606 2.5 years[64-65]), this warming trend in the NH may persist and spread over the years until
607 the perturbed SH_2O is fully depleted. Consequently, depending on ozone perturbations,
608 this longer-lasting SH_2O effect could eventually outweigh the cooling effect of SAOD in the SH.
609
610 Our findings show that the climate impact of shallow submarine eruptions (water-rich
611 eruptions with a moderate amount of SO_2) differs from that of subaerial
612 eruptions (e.g., Pinatubo[22]), depending on the injected altitude and composition of the volcanic
613 plume.

Methods

This study aimed to assess the radiative effects of the Hunga eruption. To achieve this, we analyzed observed changes in the three main radiatively important species in the stratosphere that were substantially perturbed by the eruption: water vapor, aerosols, and ozone (see Supplementary Information). We then used the observed changes in these three stratospheric species before and after the eruption to simulate the radiative effects of the Hunga eruption using the LibRadtran radiative transfer model (Supplementary Figure 1).

Descriptions of data sets

SAGE-III/ISS observations

We analyzed SAGE III/ISS data from 7 June 2017 to 31 December 2023, covering latitudes from 70°N to 70°S, depending on variations in solar insolation, solar zenith angle, and the coverage range of the ISS instrument. Specifically, we used solar occultation data from SAGE III on the ISS (SAGE III/ISS; version 5.3, accessed on 28 October 2023; Algorithm Theoretical Basis Document (ATBD)[70-71]), which provided approximately 30 atmospheric profiles per day of H_2O, O_3, and aerosol extinction coefficient at sunrise and sunset across the globe.

Compared to estimates of stratospheric temperature and composition from passive limb sounding instruments (e.g., Aura Microwave Limb Sounder; MLS), the solar occultation technique of SAGE III/ISS provides much higher vertical resolution measurements. While MLS offers daily near-global observations (82°S–82°N; Supplementary Figures 11-12), its lower vertical resolution makes it challenging to fully resolve vertical variations in SH_2O and ozone, as well as the associated radiative forcings[49-50]. From the perspective of higher vertical resolution, accurate estimation of atmospheric heating rates and top-of-atmosphere radiative forcing requires detailed profiling of radiatively active species, such as water vapor, ozone, and aerosols[49]. Therefore, in this study, we primarily use multi-wavelength SAGE III/ISS data as input for most of our radiative forcing analysis. However, we also compare our results with other satellite products, including MLS for H_2O and O_3 (Supplementary Figs. 3, 11–14) and SAOD measurements from multiple instruments, such as OMPS-SASK, OMPS-NASA, and

644 GloSSAC, to ensure consistency and to assess and highlight uncertainties across different
645 datasets (Supplementary Fig. 2; Table 1).
646
647 We analyzed approximately 70,000 profiles over our study period, conducting the
648 analysis on a seasonal basis to ensure sufficient global observations while accounting
649 for temporal changes in solar angle and other variables when calculating the radiative effects of
650 the eruption (Supplementary Methods). We computed the observed changes in SH_2O, multi-
651 wavelength aerosol extinction coefficient, and ozone as a function of altitude (binned at 0.5 km),
652 latitude (binned at 5° to ensure robust sampling statistics per bin), and longitude (binned at
653 10°). Additionally, we estimated the seasonal variations in a near-global map, depicting
654 the vertical integral of water vapor, aerosol extinction coefficient, and ozone concentration from
655 the lower to upper stratosphere.
656
657 We divided the background period before the Hunga eruption (CLIM period) into
658 four seasons: DJF (December–January–February), MAM (March–April–May), JJA (June–July–
659 August), and SON (September–October–November), using data from 7 June 2017 to 9
660 December 2021 (data was unavailable between 10–18 December 2021). We included all
661 available data from December 2021 before the initial phase of the Hunga eruption began on 19
662 December 2021. Similarly, we divided the Hunga eruption period into: Hunga-2022: JF (15
663 January – 28 February 2022), MAM (1 March – 31 May 2022), JJA (1 June – 31 August
664 2022), and SON (1 September – 30 November 2022). Hunga-2023: DJF (December 2022 – 28
665 February 2023), MAM (1 March – 31 May 2023), JJA (1 June – 31 August 2023), and SON (1
666 September – 30 November 2023).
667
668 For our radiative calculations, we applied the nearest-neighbor interpolation technique (K-
669 dimensional tree interpolation) when necessary to achieve complete latitude-longitude
670 coverage between 70°S and 70°N. Finally, we computed the weighted mean, accounting
671 for differences in the number of days across the four seasonal analysis periods during both
672 the Hunga and CLIM periods. This approach enabled us to assess annual-mean changes in
673 the radiation budget, thereby quantifying the annual radiative effect of Hunga-2022 and Hunga-
674 2023.

Ozone perturbations analysis following the Hunga Eruption: 2D-filtered anomaly

To assess ozone perturbations associated with the Hunga eruption during 2022 and 2023, we employed a structured methodology based on the approach adopted by Wilmouth[35]:

(a) **Evaluation of ozone mixing ratio anomalies exceeding 2σ**: We analyzed the zonal-mean and seasonal-mean ozone (O_3) mixing ratio in 2022 and 2023 to identify deviations exceeding ±2 standard deviations from the 2005–2021 MLS and 2017–2021 SAGE III seasonal means.

(b) **Detection of ozone anomalies exceeding 2σ, synchronized with >2σ water vapor anomalies**: The Hunga eruption strongly perturbed water vapor, meaning that any ozone changes caused by the eruption should co-occur with water vapor anomalies (Wilmouth[35]). Therefore, regions where water vapor was perturbed served as a reference to determine when and where the eruption also affected ozone.

Following Wilmouth[35], we identified concurrent anomalies in ozone and water vapor. Specifically, we assessed ozone changes as a function of season, latitude bin (5°), and pressure level for MLS (and 0.5 km altitude bin for SAGE III), ensuring that they coincided with water vapor anomalies exceeding >2σ above the MLS 16-year mean and SAGE III 5-year mean.

(c) **Removal of pre-existing anomaly values from 2022 and 2023**: To quantify ozone anomalies caused by the Hunga eruption, we examined whether the 2022–2023 anomalies had occurred in previous years and whether they fell within background variability, independent of the eruption. Using abnormally high water vapor levels in 2022 and 2023 as a reference, we identified and excluded zonal-mean ozone anomaly values (classified by season, latitude, and altitude) that predated these exceptional conditions.

(d) **Application of the 2D-Filtered (2DF) technique**: The 2D-Filtered (2DF) technique was applied to ozone anomalies as a function of season, latitude, and altitude (or pressure level) if they met the criteria from Steps (a) to (c) (Fig. 2c; Fig. 4a,b; Supplementary Figure 10, 13, 14). When the 2DF technique was applied without water vapor constraints, it was referred to as 2D-Filtered (2DF) without water vapor (see Supplementary Fig. 10). Ozone anomalies that did not meet these criteria were classified as unfiltered conditions (Supplementary Fig. 3e-h). Note that one

limitation of this filtering approach is that it may underestimate ozone anomalies influenced by secondary circulation effects that extend beyond the core of the water vapor anomalies.

Mass extinction efficiency of sulfate aerosol

Mass extinction efficiency (MEE; $m^2 g^{-1}$) of sulfate aerosols indicates how efficiently of aerosols scatter or absorb of solar radiation per unit mass. It can be expressed as:

$$MEE[m, 521nm, D_s] = \frac{\int_{D_{smin}}^{D_{smax}} \frac{3}{2\rho_s D_s} Q_{ext}(D_s, n, k, 521nm) n_M(D_s) dD_s}{\int_{D_{smin}}^{D_{smax}} n_M(D_s) dD_s} \quad (1)$$

The mass size distribution, $n_M(D_s)$, is given by:

$$n_M(D_s) = \frac{\pi}{6} \rho_s {D_s}^3 n(D_s)$$

where $n(D_s)$ represents the log-normal number size distribution at geometric standard deviation of 1.2. ρ_s is the SO_2 density. Based on the retrieved effective radius (r_{eff}) of sulfate aerosol (D_s = $2r_{eff}$) and the complex refractive index of sulfate aerosol at 521 nm (real part: n = 1.431; imaginary part: k = 1.0 x 10^{-8}), we determined the extinction efficiency factor (Q_{ext} at 521 nm) using Mie theory (Supplementary Figure 7, 8,11). Details of the expression of $Q_{ext}(r_{eff}, n, k, 521nm)$ are provided in the Supplementary Methods. The refractive index of sulfate aerosol is obtained from GEISA database.

The hemispherical mean value of MEE is also estimated using:

$$\text{MEE} = \frac{\text{SAOD} * \text{Surface area}[\text{m}^2]}{\text{mass of } SO_2[\text{g}] * \left(\frac{\frac{\text{Molar Mass of } H_2SO_4}{\text{Molar mass of } SO_2} * 1}{\text{wt}} \right)} \quad (2)$$

Here, wt is the 75% H_2SO_4 weight.

Relative and absolute changes of three stratospheric species: Hunga versus CLIM

We determined the relative and absolute changes in the three stratospheric species (Y) for the Hunga and CLIM periods using:

$$Absolute\ change = \Delta Y = Y[HTHH] - Y[CLIM] \quad (3)$$

$$\%\ Relative\ change = 100 \times \frac{\Delta Y}{Y[CLIM]} \quad (4)$$

Retrieval of optical and microphysical properties of stratospheric sulfate aerosol: Hunga versus CLIM

We utilized near-global coverage of the spatial and temporal distribution of aerosol extinction [km^{-1}] (SAGE-III; ATBD, 2002) at nine wavelengths (384.224 nm, 448.511 nm, 520.513 nm, 601.583 nm, 676.037 nm, 755.979 nm, 869.178 nm, 1021.20 nm, and 1543.92 nm). It is important to note that uncertainty in aerosol extinction varies with wavelength[70]. For instance, at 407 nm and 1089 nm, the uncertainty can exceed 25%, whereas at 450 nm, it decreases to 10%, and at 521 nm, it is less than 5%. To maximize accuracy, we jointly utilized all nine wavelengths to retrieve stratospheric sulfate aerosol optical and microphysical properties using a pre-calculated look-up table (LUT) based on Mie theory[66,71-74].

Mie-LUT based retrieval of stratospheric sulfate aerosol

An accurate assessment of the size distribution of stratospheric aerosols is crucial for accurately quantifying their radiative effects before and after the eruption. When analyzing background stratospheric aerosols, studies have shown that their size distribution can typically be characterized by a unimodal lognormal distribution[75]. These aerosols are predominantly spherical and consist of approximately 75% sulfuric acid and 25% water vapor[68-73.]

Ground-based stratospheric aerosol observations from AERONET indicate that during the early stages of aerosol growth following the Hunga eruption, bi-modal and tri-modal log-normal size distributions better represented the aerosol characteristics, particularly the coarse mode of aerosol particles[16,17]. However, within a few months after the eruption, the data showed that fine-mode stratospheric aerosols became dominant in aerosol extinction[16,67]. Thus, we

adopted a unimodal log-normal size distribution to represent the size distribution of sulfate aerosols resulting from the Hunga eruption, with a geometric standard deviation of 1.2. This is broadly consistent with the more comprehensive size distribution analysis by Knepp[66], Khaykin[66] and Duchamp[16]. This size distribution parameterization has previously been used to assess stratospheric sulfate aerosol growth one year after the Pinatubo eruption[22]. Notably, Knepp[66] introduced a novel method based on SAGE III data, indicating a spectral width of 1.2 to 1.3 post-Hunga eruption, which aligns with our choice of 1.2 for the geometric standard deviation in the Hunga case.

We used the Mie LUT to retrieve the optical and microphysical properties of sulfate aerosols from SAGE III/ISS stratospheric aerosol extinction profiles at nine wavelengths, covering the period from 7 June 2017 to 31 December 2023 (Hunga-2022 vs. CLIM and Hunga-2023 vs. CLIM periods). For this purpose, we followed these steps:

1. We calculate the aerosol extinction ratios at 521 nm as: 384.224 /520.513 nm, 448.511/520.513 nm, 520.513/520.513 nm, 601.583/520.513nm, 676.037/520.513 nm, 755.979/520.513 nm, 869.178/520.513 nm, 1021.20/520.513 nm, and 1543.92/520.513 nm) using SAGE-III/ISS observations.

2. We compare the SAGE-III aerosol extinction ratios (from point 1) with the Mie LUT aerosol extinction ratios and determine the closest matching extinction ratios at each given wavelength.
3. We calculate the squared difference between the eight aerosol extinction ratios from SAGE-III/ISS and the Mie LUT for each effective radius, then sum these differences to quantify the discrepancy between the two datasets.

Here, Eq. (5) summarizes above step 3:

$$p(r_{eff}) = \sum_{\lambda_i} \left[Q_{ratio_{SAGE}}(\lambda_i) - Q_{ratio_{LUT}}(\lambda_i, r_{eff}) \right]^2 \quad (5)$$

where $Q_{ratio,_{SAGE}}$ and $Q_{ratio_{LUT}}$ represent the extinction ratio at 521 nm from SAGE-III observations and LUT, respectively. Here λ_i sums over the eight wavelengths from 400

to 1450 nm (as listed above), determined for both SAGE-III and LUT table using interpolation techniques.

4. The minimum sum of squared differences represents the best solution for the effective radius, asymmetry factor, and single scattering albedo. This step identifies the closest match between the observed and modeled data.

Simulations of radiative effects of three stratospheric species (Hunga versus CLIM periods) | Columnar- & Zonal-mean

We utilized observational data from multiple instruments (SAGE III/ISS and Aura MLS) to obtain atmospheric and aerosol extinction profiles. Specifically, we retrieved vertical profiles of temperature, pressure, density, water vapor (H_2O), ozone (O_3), and multi-wavelength aerosol extinction from SAGE III/ISS observations between 9 km and 100 km altitude. For atmospheric profiles below 9 km, we incorporated data from other sources, including MLS[58] and ERA5[78].

Using the input data described above, we conducted idealized radiative transfer simulations to examine the 3D distribution of stratospheric radiative heating rates and instantaneous radiative fluxes between two periods: Hunga-2022 and Hunga-2023 versus the CLIM period, at the TOA and near the tropopause. A summary of these data sources and radiative transfer model simulations is provided in Supplementary Figure 1. Using the LibRadtran model with the DISORT solver[59,79-80] and eight streams, we simulated radiative flux changes and associated heating rates by incorporating observed seasonal-mean vertical profiles of atmospheric constituents, aerosol properties, and seasonal-mean daily-insolation weighted solar zenith angle as a function of latitude and longitude. These simulations were conducted separately for the shortwave (0.28–4 μm) and longwave (4.0–100 μm) components of radiative flux changes and heating rates (see Supplementary Methods). We used the CLIM period to define the atmospheric temperature profiles (per season) and applied these fixed temperature profiles for the Hunga period analysis. Thus, our radiative calculations do not account for any temperature adjustments in the stratosphere in the year following the eruption due to net heating/cooling from different radiative species. This analysis design allows us

to clearly isolate the instantaneous radiative response of the Hunga eruption from eruption-associated climate feedbacks (e.g., dynamical changes) that influence the observed stratospheric and tropospheric temperature profiles over the past year.

Uncertainty analysis related to three stratospheric species

We estimated seasonal and yearly standard deviation values for three stratospheric species (H_2O, sulfate aerosol, and O_3) using SAGE III/ISS observations from 2017 to 2021, before the Hunga eruption. Based on these yearly standard deviation values of the perturbed stratospheric species, we calculated the corresponding standard deviation associated with their instantaneous radiative effects at the TOA and near the tropopause (Fig. 2). Additionally, we determined the propagated standard deviation for the combined radiative effects of the three stratospheric species (Fig. 2). It is important to note that the standard deviation associated with surface temperature changes, estimated using the FaIR model[7-8], is derived from the propagated standard deviation of the combined instantaneous radiative effects of the three stratospheric species[66]. We presented the standard deviation values rounded to two and three places. Other sources of uncertainty, such as dynamical variations, cloud effects, and biases across different satellite products, may also influence temperature changes. However, these factors are beyond the scope of this study and are therefore not included in our uncertainty estimate[66].

Limitations of Radiative transfer model

Even though we directly use the observed vertical profiles of aerosols, stratospheric water vapor, and ozone as inputs to the LibRadtran model, our results are subject to several important limitations.

First, the infrequent sampling of aerosol extinction profiles at multiple wavelengths by SAGE III introduces uncertainties in SAOD retrievals, particularly in the lower stratosphere following the Hunga eruption. Thus, cross-instrument comparisons are critical for improving confidence in SAOD estimates and reducing uncertainties in radiative forcing assessments following major volcanic events (Supplementary Figure 2 and Supplementary Table 1).

Second, the high signal-to-noise ratio SAGE-III/ISS dataset we used provides only dawn-dusk solar stratospheric profiles. Consequently, we cannot capture the diurnal variations of radiative fluxes in our calculations, which are limited to daytime periods (i.e., no diurnal variability is considered). However, we anticipate that this limitation does not significantly affect our results, as the impact of diurnal temperature and water vapor variations in the stratosphere is relatively small[81-84].

Third, for computational simplicity, we assume a fixed, idealized clear-sky surface albedo of 0.15 between 60°N and 60°S (Supplementary Figure 15). This assumption may influence the net magnitude of the cooling effect, which could be even stronger if surface albedo were higher. However, the overall sign of the radiative effect remains the same even if the clear-sky surface albedo is assumed to be 0.2 over the same latitude range.

Fourth, our idealized radiation-only simulations do not account for the dynamical effects of radiative components. Additionally, we do not incorporate measured temperature profiles from the Hunga eruption period to estimate radiative forcing under a relaxed stratospheric state (i.e., effective radiative forcing). Notably, Schoeberl[15] accounted for temperature anomalies and found that while they are not always as pronounced as those associated with water vapor or aerosols, they are non-negligible. To illustrate the potential impact of stratospheric temperature anomalies (cooling), we provide idealized radiative forcing column calculations in Supplementary Figures 15–19, showing that these anomalies primarily affect longwave radiation. When accounting for stratospheric temperature changes, we find that the radiative forcing at both the TOA and near the tropopause altitude due to stratospheric water vapor remains positive. Furthermore, surface albedo should ideally be treated as a dynamic variable, varying with surface type, land use, and seasonal changes. Nonetheless, despite these simplifications, our primary conclusion—that sulfate aerosols dominate the stratospheric radiative cooling effect among the three species considered—remains robust.

The Finite-amplitude Impulse-Response (FaIR) model

We use the Finite-Amplitude Impulse-Response (FaIR) model, an emulator of a two-layer energy balance system, to estimate the first-order temperature response to the Hunga

eruption[7–8]. In this model, "finite-amplitude" refers to the response magnitude being determined by the forcing strength, while "impulse-response" describes the system's reaction to a sudden forcing change. FaIR is applied to assess the temperature response to Hunga-induced radiative forcing from stratospheric water vapor, sulfate aerosols, and ozone. The model provides an estimate of the resulting temperature change, particularly in the SH. However, as FaIR primarily simulates global and hemispheric-scale surface temperature changes, it does not fully account for regional variability or all Earth system feedbacks.

Data availability

The SAGE-III/ISS v053 solar datasets (filename: g3bssp_53) are freely available from (https://asdc.larc.nasa.gov/project/SAGE%20III-ISS/g3bssp_53). The Aura MLS dataset is also freely available and can be obtained using https://search.earthdata.nasa.gov/. The ECMWF ERA5 reanalysis pressure level datasets can be obtained from https://cds.climate.copernicus.eu/cdsapp#!/search?type=dataset. Underlying data (Supplementary Data 1-5) related to the manuscript is publicly available at Zenodo website (https://zenodo.org/records/14955808 ; Gupta[85]). The data related to the refractive index of sulfate aerosols is taken from https://geisa.aeris-data.fr/litms/. The Mie table for sulfate aerosol is available here: https://github.com/matthew2e/easy-volcanic-aerosol/blob/master/eva_Mie_lookuptables.nc[72].

Code availability

The LibRadtran model is available at http://www.libradtran.org/doku.php?id=download here. All the Figures (including Supplementary Figures) were originally produced and plotted using various open-source Python libraries (e.g., https://matplotlib.org/stable/). The LibRadtran model-based processed data and input is also publicly available at the Zenodo (https://zenodo.org/records/14955808; Gupta[85]).

References

1. Millan, L. et al. The Hunga Tonga-Hunga Ha'apai hydration of the stratosphere. *Geophys. Res. Lett.* 49, e2022GL099381 (2022).

2. Gupta, A. K., Bennartz, R., Fauria, K. E. & Mittal, T. Eruption chronology of the December 2021 to January 2022 Hunga Tonga-Hunga Ha'apai eruption sequence. *Commun. Earth Environ.* 3(1), 314 (2022).

3. Self, S., Zhao, J. X., Holasek, R. E., Torres, R. C. & King, A. J. The atmospheric impact of the 1991 Mount Pinatubo eruption (No. NASA/CR-93-207274). *NASA Report* (1993).

4. Carn, S. A., Krotkov, N. A., Fisher, B. L. & Li, C. Out of the blue: Volcanic SO_2 emissions during the 2021–2022 eruptions of Hunga Tonga—Hunga Ha'apai (Tonga). *Front. Earth Sci.* 10, 976962 (2022).

5. Jenkins, S., Chris, S., Myles, A. & Roy, G. Tonga eruption increases chance of temporary surface temperature anomaly above 1.5° C. *Nat. Clim. Change* 13(2), 127–129 (2023).

6. Zhu, Y. et al. Perturbations in stratospheric aerosol evolution due to the water-rich plume of the 2022 Hunga-Tonga eruption. *Commun. Earth Environ.* 3(1), 248 (2022).

7. Smith, C. J. et al. FAIR v1.3: A simple emissions-based impulse response and carbon cycle model. *Geosci. Model Dev.* 11(6), 2273–2297 (2018).

8. Held, I. M. et al. Probing the fast and slow components of global warming by returning abruptly to preindustrial forcing. *J. Clim.* 23(9), 2418–2427 (2010).

9. Vömel, H., Evan, S. & Tully, M. Water vapor injection into the stratosphere by Hunga Tonga-Hunga Ha'apai. *Science*377(6613), 1444–1447 (2022).

10. Global Volcanism Program (GVP). Report on Hunga Tonga-Hunga Ha'apai (Tonga). In S. K. Sennert (ed.), *Weekly Volcanic Activity Report*, 16 February–22 February 2022. Smithsonian Institution and US Geological Survey (2022).

11. Xu, J., Li, D., Bai, Z., Tao, M. & Bian, J. Large amounts of water vapor were injected into the stratosphere by the Hunga Tonga–Hunga Ha'apai volcano eruption. *Atmosphere* 13, 912 (2022).

12. Sellitto, P. et al. The unexpected radiative impact of the Hunga Tonga eruption of 15 January 2022. *Commun. Earth Environ.* 1, 288 (2022).

13. Schoeberl, M. et al. Analysis and impact of the Hunga Tonga-Hunga Ha'apai stratospheric water vapor plume. *Geophys. Res. Lett.* 49(20), e2022GL100248 (2022).

14. Schoeberl, M. The estimated climate impact of the Hunga Tonga-Hunga Ha'apai eruption plume. *Geophys. Res. Lett.* 50, e2023GL104634 (2023).

15. Schoeberl, M. R. Evolution of the climate forcing during the two years after the Hunga Tonga-Hunga Ha'apai eruption. *J. Geophys. Res. Atmos.* 129, e2024JD041296 (2024).

16. Duchamp, C. et al. Observation of the aerosol plume from the 2022 Hunga Tonga—Hunga Ha'apai eruption with SAGE III/ISS. *Geophys. Res. Lett.* 50(18), e2023GL105076 (2023).

17. Boichu, M. et al. Growth and global persistence of stratospheric sulfate aerosols from the 2022 Hunga Tonga–Hunga Ha'apai volcanic eruption. *J. Geophys. Res. Atmos.* 128(23), e2023JD039010 (2023).

18. Forster, P. M. D. F. & Shine, K. P. Assessing the climate impact of trends in stratospheric water vapor. *Geophys. Res. Lett.* 29(6), 10–1 (2002).

19. Solomon, S. et al. Contributions of stratospheric water vapor to decadal changes in the rate of global warming. *Science* 327(5970), 1219–1223 (2010).

20. Fueglistaler, S. & Haynes, P. H. Control of interannual and longer-term variability of stratospheric water vapor. *J. Geophys. Res. Atmos.* 110 (D24) (2005).

21. Bergstrom, R. W., Kinne, S., Russell, P. B., Bauman, J. J. & Minnis, P. Radiative forcing of the Pinatubo aerosol as a function of latitude and time. *NASA Technical Report* (1996).

22. Stenchikov, G. L. et al. Radiative forcing from the 1991 Mount Pinatubo volcanic eruption. *J. Geophys. Res. Atmos.*103(D12), 13837–13857 (1998).

23. Witze, A. Why the Tongan eruption will go down in the history of volcanology. *Nature* 602, 376–378 (2022).

24. Oppenheimer, C. Climatic, environmental and human consequences of the largest known historic eruption: Tambora volcano (Indonesia) 1815. *Prog. Phys. Geogr.* 27(2), 230–259 (2003).

25. Hand, J. L. & Malm, W. C. Review of aerosol mass scattering efficiencies from ground-based measurements since 1990. *J. Geophys. Res. Atmos.* 112 (D16) (2007).

26. Lu, J. et al. Stratospheric aerosol and ozone responses to the Hunga Tonga-Hunga Ha'apai volcanic eruption. *Geophys. Res. Lett.* 50(4), e2022GL102315 (2023).

27. Carslaw, K. S. et al. Stratospheric aerosol growth and HNO_3 gas phase depletion from coupled HNO_3 and water uptake by liquid particles. *Geophys. Res. Lett.* 21(23), 2479–2482 (1994).

28. Solomon, S., Garcia, R. R., Rowland, F. S. & Wuebbles, D. J. On the depletion of Antarctic ozone. *Nature*321(6072), 755–758 (1986).

29. Shine, K. P., Byrom, R. E. & Checa-Garcia, R. Separating the shortwave and longwave components of greenhouse gas radiative forcing. *Atmos. Sci. Lett.* 23(10), e1116 (2022).

30. Coy, L. Stratospheric circulation changes associated with the Hunga Tonga-Hunga Ha'apai eruption. *Geophys. Res. Lett.* 49(22), e2022GL100982 (2022).

31. Raymond, N., Bernath, P. & Boone, C. Atmospheric effects of the Tonga volcanic sulfate aerosols. *J. Quant. Spectrosc. Radiat. Transfer* (2024): 109056.

32. Zhang, J. et al. Chemistry contribution to stratospheric ozone depletion after the unprecedented water-rich Hunga Tonga eruption. *Geophys. Res. Lett.* 51(7), e2023GL105762 (2024).

33. Maycock, A. C., Smith, C. J., Rap, A. & Rutherford, O. On the structure of instantaneous radiative forcing kernels for greenhouse gases. *J. Atmos. Sci.* 78(3), 949–965 (2021).

34. Basha, G. et al. Impact of Hunga Tonga-Hunga Ha'apai volcanic eruption on stratospheric water vapour, temperature, and ozone. *Remote Sens.* 15(14), 3602 (2023).

35. Wilmouth, D. M. et al. Impact of the Hunga Tonga volcanic eruption on stratospheric composition. *Proc. Natl. Acad. Sci. USA* 120(46), e2301994120 (2023).

36. Wang, X. et al. Stratospheric climate anomalies and ozone loss caused by the Hunga Tonga-Hunga Ha'apai volcanic eruption. *J. Geophys. Res. Atmos.* 128(22), e2023JD039480 (2023).

37. Santee, M. L. et al. Strong evidence of heterogeneous processing on stratospheric sulfate aerosol in the extrapolar southern hemisphere following the 2022 Hunga Tonga-Hunga Ha'apai eruption. *J. Geophys. Res. Atmos.* 128(16), e2023JD039169 (2023).

38. Asher, E. et al. Unexpectedly rapid aerosol formation in the Hunga Tonga plume. *Proc. Natl. Acad. Sci. USA*120(46), e2219547120 (2023).

39. Legras, B. et al. The evolution and dynamics of the Hunga Tonga–Hunga Ha'apai sulfate aerosol plume in the stratosphere. *Atmos. Chem. Phys.* 22(22), 14957–14970 (2022).

40. Fleming, E. L., Newman, P. A., Liang, Q. & Oman, L. D. Stratospheric temperature and ozone impacts of the Hunga Tonga-Hunga Ha'apai water vapor injection. *J. Geophys. Res. Atmos.* 129(1), e2023JD039298 (2024).

41. Erba, E. et al. Environmental consequences of Ontong Java Plateau and Kerguelen plateau volcanism. *Geol. Soc. Am. Spec. Pap.* 511, 271–303 (2015).

42. Kump, L. R. & Barley, M. E. Increased subaerial volcanism and the rise of atmospheric oxygen 2.5 billion years ago. *Nature* 448(7157), 1033–1036 (2007).

43. Li, Chenwei et al. Microphysical simulation of the 2022 Hunga volcano eruption using a sectional aerosol model. *Geophys. Res. Lett.* 51(11), e2024GL108522 (2024).

44. Madhavan, B. L. et al. Stratospheric aerosol characteristics from the 2017–2019 volcanic eruptions using the SAGE III/ISS observations. *Remote Sens.* 15(1), 29 (2022).

45. Schallock, J. Reconstructing volcanic radiative forcing since 1990 using a comprehensive emission inventory and spatially resolved sulfur injections from satellite data in a chemistry-climate model. *Atmos. Chem. Phys.* 23(2), 1169–1207 (2023).

46. Wang, Y. & Huang, Y. Compensating atmospheric adjustments reduce the volcanic forcing from Hunga stratospheric water vapor enhancement. *Sci. Adv.* 10(32), eadl2842 (2024).

47. Thomason, L. W. & Taha, G. SAGE III aerosol extinction measurements: Initial results. *Geophys. Res. Lett.* 30(12) (2003).

48. Thomason, L. W., Moore, J. R., Pitts, M. C., Zawodny, J. M. & Chiou, E. W. An evaluation of the SAGE III version 4 aerosol extinction coefficient and water vapor data products. *Atmos. Chem. Phys.* 10(5), 2159–2173 (2010).

49. Ramanathan, V. et al. Warming trends in Asia amplified by brown cloud solar absorption. *Nature* 448, 575–578 (2007).

50. Davis, S. M. et al. Validation of SAGE III/ISS solar water vapor data with correlative satellite and balloon-borne measurements. *J. Geophys. Res. Atmos.* 126(2), e2020JD033803 (2021).

51. Strode, S. A. SAGE III/ISS ozone and NO_2 validation using diurnal scaling factors. *Atmos. Meas. Tech.* 15(20), 6145–6161 (2022).

52. Park, M. et al. . *J. Geophys. Res. Atmos.* 126(7), e2020JD034274 (2021).

53. Taha, G. et al. OMPS LP version 2.0 multi-wavelength aerosol extinction coefficient retrieval algorithm. *Atmos. Meas. Tech.* 14(2), 1015–1036 (2021).

54. Rozanov, A. et al. Retrieval of stratospheric aerosol extinction coefficients from sun-normalized Ozone Mapper and Profiler Suite Limb Profiler (OMPS-LP) measurements. *Atmos. Meas. Tech.* 17(22), 6677–6695 (2024).

55. Chen, Z., Bhartia, P. K., Loughman, R., Taha, G. & Xu, P. Evaluation of the OMPS/LP stratospheric aerosol extinction product using SAGE III/ISS observations. *Atmos. Meas. Tech.* 13(6), 3471–3485 (2020).

56. Kovilakam, M. et al. OMPS-LP aerosol extinction coefficients and their applicability in GloSSAC. *EGUsphere*2024, 1–31 (2024).

57. Damadeo, R. P., Sofieva, V. F., Rozanov, A. & Thomason, L. W. An empirical characterization of the aerosol Ångström exponent interpolation bias using SAGE III/ISS data. *Atmos. Meas. Tech.* 17(12), 3669–3678 (2024).

58. Waters, J. W. et al. The earth observing system microwave limb sounder (EOS MLS) on the Aura satellite. *IEEE Trans. Geosci. Remote Sens.* 44(5), 1075–1092 (2006).

59. Mayer, B. & Kylling, A. The libRadtran software package for radiative transfer calculations—description and examples of use. *Atmos. Chem. Phys.* 5(7), 1855–1877 (2005).

60. Sellitto, P. et al. Observing the SO_2 and sulfate aerosol plumes from the 2022 Hunga eruption with the Infrared Atmospheric Sounding Interferometer (IASI). *Geophys. Res. Lett.* 51(19), e2023GL105565 (2024).

61. de Leeuw et al. The 2019 Raikoke volcanic eruption—Part 1: Dispersion model simulations and satellite retrievals of volcanic sulfur dioxide. *Atmos. Chem. Phys.* 21(14), 10851–10879 (2021).

62. Timmreck, C. et al. The interactive stratospheric aerosol model intercomparison project (ISA-MIP): Motivation and experimental design. *Geosci. Model Dev.* 11(7), 2581–2608 (2018).

63. Stenchikov, G. et al. How does a Pinatubo-size volcanic cloud reach the middle stratosphere? *J. Geophys. Res. Atmos.* 126(10), e2020JD033829 (2021).

64. Toohey, M., Jia, Y., Khanal, S. & Tegtmeier, S. Stratospheric residence time and the lifetime of volcanic stratospheric aerosols. *EGUsphere* 2024, 1–28 (2024).

65. Hamill, P., Jensen, E. J., Russell, P. B. & Bauman, J. J. The life cycle of stratospheric aerosol particles. *Bull. Am. Meteorol. Soc.* 78(7), 1395–1410 (1997).

66. Knepp, T. N., Kovilakam, M., Thomason, L. & Miller, S. J. Characterization of particle size distribution uncertainties using SAGE II and SAGE III/ISS extinction spectra. *Atmos. Meas. Tech. Discuss.* 2023, 1–42 (2023).

67. Khaykin, S. et al. Global perturbation of stratospheric water and aerosol burden by Hunga eruption. *Commun. Earth Environ.* 3(1), 316 (2022).

68. Marshall, L. et al. Multi-model comparison of the volcanic sulfate deposition from the 1815 eruption of Mt. Tambora. *Atmos. Chem. Phys.* 18(3), 2307–2328 (2018).

69. Schmidt, A. et al. Volcanic radiative forcing from 1979 to 2015. *J. Geophys. Res. Atmos.* 123(22), 12491–12508 (2018).

70. SA, E. SAGE III. Available at: https://eospso.gsfc.nasa.gov/sites/default/files/atbd/atbd-sage-cloud.pdf (2002).

71. Wrana, F., von Savigny, C., Zalach, J. & Thomason, L. W. Retrieval of stratospheric aerosol size distribution parameters using satellite solar occultation measurements at three wavelengths. *Atmos. Meas. Tech.* 14(3), 2345–2357 (2021).

72. Aubry, T. J., Toohey, M., Marshall, L., Schmidt, A. & Jellinek, A. M. A new volcanic stratospheric sulfate aerosol forcing emulator (EVA_H): Comparison with interactive stratospheric aerosol models. *J. Geophys. Res. Atmos.* 125(3), e2019JD031303 (2020).

73. Toohey, M., Stevens, B., Schmidt, H. & Timmreck, C. Easy Volcanic Aerosol (EVA v1.0): An idealized forcing generator for climate simulations. *Geosci. Model Dev.* 9(11), 4049–4070 (2016).

74. Wrana, F., Niemeier, U., Thomason, L. W., Wallis, S. & von Savigny, C. Stratospheric aerosol size reduction after volcanic eruptions. *Atmos. Chem. Phys.* 23(17), 9725–9743 (2023).

75. Kahn, R. A. et al. Evolving particles in the 2022 Hunga Tonga—Hunga Ha'apai volcano eruption plume. *J. Geophys. Res. Atmos.* 129(11), e2023JD039963 (2024).

76. Kremser, S. et al. Stratospheric aerosol—Observations, processes, and impact on climate. *Rev. Geophys.* 54(2), 278–335 (2016).

77. Palmer, K. F. & Williams, D. Optical constants of sulfuric acid; application to the clouds of Venus? *Appl. Opt.* 14(1), 208–219 (1975).

78. Hersbach, H. et al. The ERA5 global reanalysis. *Q. J. R. Meteorol. Soc.* 146, 1999–2049 (2020).

79. Gasteiger, J. et al. Representative wavelengths absorption parameterization applied to satellite channels and spectral bands. *J. Quant. Spectrosc. Radiat. Transfer* 148, 99–115 (2014).

80. Stamnes, K., Tsay, S. C., Wiscombe, W. & Laszlo, I. DISORT, general-purpose Fortran program for discrete-ordinate-method radiative transfer in scattering and emitting layered media: Documentation of methodology. *Tech. Rep.*(2000).

81. Haywood, J. M. & Shine, K. P. The effect of anthropogenic sulfate and soot aerosol on the clear sky planetary radiation budget. *Geophys. Res. Lett.* 22(5), 603–606 (1995).

82. Baker, D. N. & Kanekal, S. G. Solar cycle changes, geomagnetic variations, and energetic particle properties in the inner magnetosphere. *J. Atmos. Sol.-Terr. Phys.* 70(2–4), 195–206 (2008).

83. Bellouin, N. et al. Radiative forcing of climate change from the Copernicus reanalysis of atmospheric composition. *Earth Syst. Sci. Data* 12(3), 1649–1677 (2020).

84. Haefele, A. et al. Diurnal changes in middle atmospheric H_2O and O_3: Observations in the Alpine region and climate models. *J. Geophys. Res. Atmos.* 113(D17) (2008).

85. Gupta, A. K. et al. The January 2022 Hunga eruption cooled the southern hemisphere in 2022 and 2023. Zenodo. https://zenodo.org/records/14955808 (2025).

Acknowledgments

We thank John Rausch for his assistance in obtaining the dataset and for his valuable discussions. We also thank Ralph Kahn for his constructive feedback and comments during scientific meetings. K. E. F. and R. B. secured funding from the National Aeronautics and Space Administration (NASA). This work was supported by NASA grant 80NSSC20K1450 awarded to the P.I. (K.E.F.) and Co-I (R.B.). A.G. received partial support from this funding during his postdoctoral tenure at Vanderbilt, and additional support from NSF grant 2151093 awarded to J. F. K. at UCLA during his current tenure at AOS, UCLA. The scope of these awards addresses submarine volcanism and the radiative effects of volcanic aerosols. We also thank the SAGE-III/ISS, LibRadtran, GEISA, and NASA teams for providing access to their data and model archives.

Author contributions

A.G. contributed to the conceptual development of this work, conducted the analysis, and produced all figures and results. R.B. ran the FaIR model. A.G. drafted the original manuscript, which was reviewed by T.M., J.F.K., R.B., and K.E.F.

Competing interests

The authors declare no competing interests.